2018 IEEE International Conference on Robotics and Automation (ICRA)
May 21-25, 2018, Brisbane, Australia

Hall Effect Sensing Workspace Estimation with Non-Permanent Magnetic Needle for Eye Anesthesia Training System via Robotic Experiments

Korn Borvorntanajanya, Jackrit Suthakorn, Ph.D., *Member, IEEE*

***Abstract*— Ophthalmic anesthesia is an important preparation for eye surgery. The conventional practice is performed blind in a cadaver under the supervision of an experienced surgeon. This paper introduces a needle tip tracking system for ophthalmic anesthesia training without major modification of an anesthesia needle. The study presents a prototyped system to track a magnetized needle tip using Hall-effect sensor array. The orbital structure model was embedded with Hall-effect sensors after considering the sensing workspace and ophthalmic anesthesia pathway. The extended Kalman filter was used to calculate needle tip position. A commercial robotic manipulator was used to model the characteristics of sensor and accuracy of the developed system. A prototype can detect needle tip position with a root-mean-square deviation around 1.80 mm. As a result, the system is capable of providing needle tip positions for training purposes.**

I. Introduction

Eye anesthesia is an important preparation for eye surgery. Since 1990 the standard technique of local anesthesia for cataract surgery has been the retrobulbar block [1], [2]. The purposes of retrobulbar block are to access and anesthetize the retrobulbar space, the area located in the middle of lateral rectus, inferior rectus and optic nerve. Failures in retrobulbar block cause complications: for example, retrobulbar hemorrhage, globe perforation, and brainstem hemorrhage [3]-[5]. Although the complication rate is rare with expert physicians, medical reports show inexperienced physicians have a complication rate of almost 4 percent [4], [5]. Eye anesthesia training uses a soft cadaver, but this provides no feedback to the trainee. The correct procedure comes only from suggestions by experienced physicians without any evidence.

Many training systems have been developed for the purposes of decreasing human error and increasing efficiency of training systems [6], [7]. The ophthalmic retrobulbar injection simulator (ORIS) provides needle position as feedback using the embedded ultrasonic sensors in a manikin's skull [8]. Needle tip position is acquired from the sensing data and the sensor positions. The ophthalmic anesthesia simulation system (OASiS) introduced the electric field based tracking system to provide position feedback of the modified needle in the orbital structure. This work has been done by a research group from Indian Institute of Technology Madras [9], [10]. A 3D model of the orbital structure and extraocular muscles have been embedded with capacitive sensors. The system captures the changes in amplitude and phase. However, the ORIS system cannot provide accurate feedback when there is an obstacle between the needle and the intended target area. Otherwise, the electric field based system is unable to detect a non-modified needle. It has to integrate with an electronic circuit.

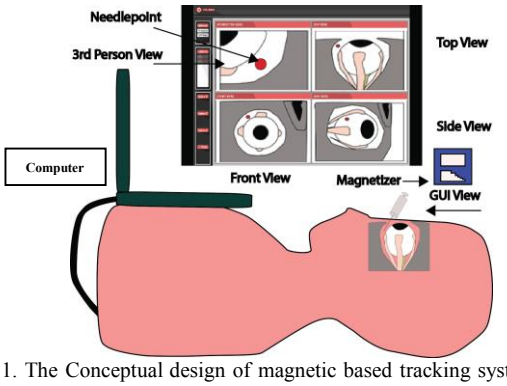

Fig. 1. The Conceptual design of magnetic based tracking system for eye anesthesia training system.

Our training system has been developed to detect a needle tip in the retrobulbar space, even it is behind an obstacle without any major modification to the anesthesia needle. The magnetic field based tracking system is one of the best solutions for the requirements [11], [12]. The advantages in non-contact detection and workspace are appropriate for the eye anesthesia training system. Our previous work was developed with the commercial passive magnetic tracking system (NDI Aurora V2 System). However, there were disadvantages in system size, modification of needle (with passive sensor), and disturbance with metallic parts. It was also hard to deploy in remote areas due to system costs. The current system has been developed with an active magnetic

*Research supported by Research Development and Engineering, RDE funds NSTDA Thailand.

Korn Borvorntanajanya is master degree student with Center for Biomedical and Robotics Technology, Faculty of Engineering, Mahidol University, 25/25 Puttamonthon 4 Road, Salaya, Nakorn Pathom 73170, Thailand, email: korn.bov@gmail.com, Phone +6684-535-9279

Jackrit Suthakorn, Ph.D. (Corresponding Author) is with the Department of Biomedical Engineering, and the Center for Biomedical and Robotics Technology (www.bartlab.org), Faculty of Engineering, Mahidol University, 25/25 Phuttamonton 4 Road, Salaya, Nakorn Pathom 73170, Thailand email: jackrit.sut@mahidol.ac.th, Thailand Phone: +662-441-4250, Fax: +662-441-9500

based sensing system [13]. The procedure is to magnetize free ions in a needle, which can be detected by a Hall-effect sensor. The sensing data is calculated to localize a needle tip. This paper presents characterization experiments between a magnetized needle and Hall-effect sensors, which can be applied to the novel position tracking system for a non-modified needle in medical applications.

II. Materials and Methods

A. Principle of Magnetized Needle and Hall-Effect Sensor

An anesthesia needle is a hollow cylindrical tube as shown in Fig. 2a. The characteristic of magnetic flux density (B) from a cylindrical shape is known as a dipole model [11], [12]. The ring-shaped model is selected from the shape of a hollow tube.

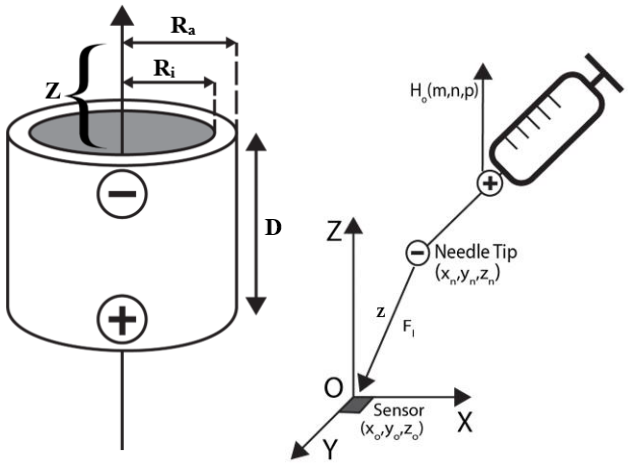

(a) (b)

Fig. 2. The magnetic pole model of magnetized needle with the ring-shaped model (a). The frame diagram between magnetic ions on needle tip (x_n, y_n, z_n) and target coordinates (x_o, y_o, z_o) (b).

The magnetic flux density (B_l) at the sensor position from the needle tip is expressed as Equation (1).

$$B_l = B_{lx}i + B_{ly}j + B_{lz}k$$

$$B_l = \frac{B_T}{2}\left[\frac{D+z}{\sqrt{R_a^2+(D+z)^2}} - \frac{z}{\sqrt{R_a^2+z^2}} + \right.$$

$$\left. - \left(\frac{D+z}{\sqrt{R_i^2+(D+z)^2}} - \frac{z}{\sqrt{R_i^2+z^2}}\right)\right] \quad (1)$$

In Equation (1), D represents height of a needle. Z is the distance between the needle tip and target area, R_a and R_i are outside and inside radius of the needle. B_T is a magnetic constant parameter, which varies with type of material. The needle materials are a composite of ferromagnetic materials, which can be magnetized. However, the magnetic constant of composite materials is unknown. Therefore, three experiments were carried out to find the magnetization constant, magnetization period and workspace due to a Hall-effect sensor.

A Hall-effect sensor is a magnetic based transducer that varies the sensing output in response to changes in magnetic field. The Hall-effect model A1324 from Allegro Micro System Company was used in this study [14]. The Hall-effect sensor has Hall sensitivity of 5 mV/Gauss (R_H) with a 5-V supply (V_s). The RoboteQ model SDC2130 is selected to convert sensing data to digital (12-bit ADC).

B. Experiments for Magnetized Needle Characterization

A robot manipulator (MOTOMAN YR-HP3-A00) was used to provide precise positions of the needle tip in this study. The needle was magnetized and attached at the end effector of a robot manipulator as in Fig. 3a. The transformation matrix was involved to calculate needle tip position related to Hall-effect sensor.

$$P_S\ {}^{S}T_N^k = P_R^k\ {}^{R}T_N \quad (2)$$

A sensor was attached with fixed table (P_S), P_N refers to position of needle tip from tool-tip calibration at the end of the effector (P_R) as in Fig. 3b. ${}^{S}T_N^k$ is the transformation matrix between the needle tip and the Hall-effect sensor at time k. ${}^{R}T_N$ represents a tool-tip calibration. P_R^k represents the position of robot manipulator at time k.

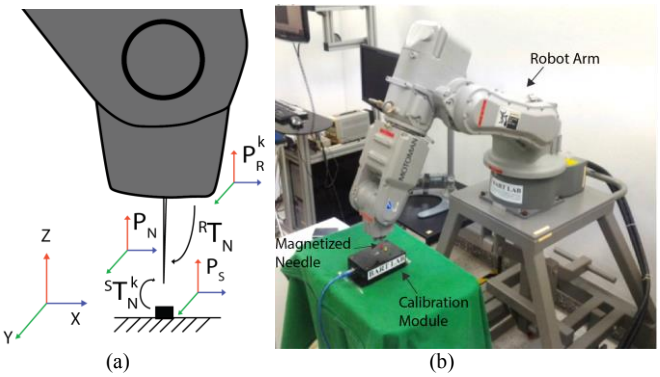

(a) (b)

Fig. 3. The characterization experiment between the Hall-effect sensor and magnetized needle using robot arm. Transformation diagram for the robot arm and Hall-effect sensor (a). The robot manipulator and calibration module for characterization experiment (b).

In the experiment, needle tip position was initiated at sensor position as a reference frame. Commands were sent to the robot manipulator to move the needle tip in a vertical direction (z-axis) in relation to the sensor from 0.0 mm to 14.0 mm (1 mm per step). In each step, data was sampled 10 times. We used the average value of sensing data to calculate a magnetic flux density from the magnetized needle. The experiment was repeated 50 times with new magnetized needles. The standard deviation and means of sensing data from different needles are listed in Table I.

The result shows that changes magnetized needles do not affect sensing values (at all distances with $P<0.05$). The magnetic intensity varies with distances according to the dipole model (1). Therefore, 13 mm is the maximum detection range of our system.

TABLE I
MEAN(SD) OF DISTANCES AND MAGNETIC FLUX DENSITY OF 50 MAGNETIZED NEEDLES (N=50)

Distance (mm)	Mean (Gauss)	SD
0.0	60.420 G	0.5144
1.0	43.551 G	0.5164
2.0	28.636 G	0.5477
3.0	17.908 G	0.5345
4.0	14.835 G	0.5450
5.0	11.468 G	0.5536
6.0	8.645 G	0.5345
7.0	7.529 G	0.5780
8.0	6.100 G	0.5536
9.0	5.400 G	0.5780
10.0	5.054 G	0.5536
11.0	4.823 G	0.5780
12.0	4.522 G	0.5536
13.0	4.311 G	0.5477
14.0	2.566 G	0.8953

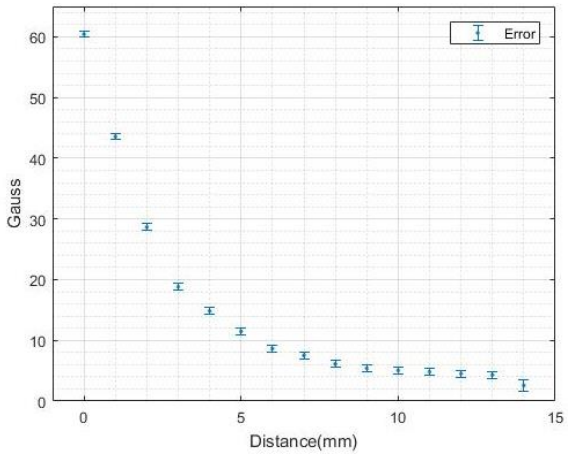

Fig. 4. Mean and SD (Error Bar) in the sensing data versus distances in the study of 50 magnetized needles.

The second experiment was designed to measure the magnetization period of the magnetized needle. A robot manipulator held the magnetized needle at 3 mm, 6 mm, and 9 mm perpendicular distance to the sensor. The Hall-effect voltage was captured every 1 minute for 2 hours. Fig. 5 shows the magnetization period of the needle. The result shows that the magnetization period is longer than operation time for eye anesthesia.

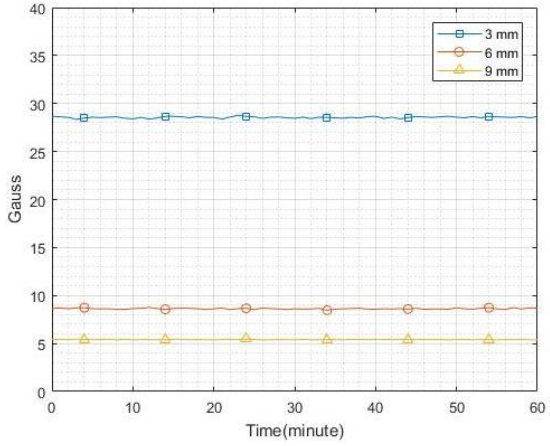

Fig. 5. The sensing data of Hall-effect sensor versus time. 3 mm distance, 6 mm distance and 9 mm distance for 2 hours.

C. Experiments for Workspace Determination

The third experiment approached the issue of determining the workspace shape between sensor and magnetized needle. The robot manipulator was commanded to move in a hemispherical shape around the sensor. The distance varied from 0 mm to 13 mm (1 mm per step) as shown in Fig. 6a. and 6b. The needle tip was initiated using the sensor position as a reference point. Sensing data was sampled 20 times for each coordinate. Experiments were repeated 20 times with the same command set. FIR low pass filter was used to reduce signal to noise ratio. Then data was applied with a thresholding filter to determine the sensing workspace. The threshold classification is defined as (3).

$$T(x) = \begin{cases} Activated\ sensor, if\ x > Threshold \\ Inactivated\ sensor, if\ x \leq Threshold \end{cases} \quad (3)$$

where (x) is sensing data of the Hall-effect sensor.

The threshold was set to 4 Gauss as a result of the first experiment. Workspaces of the sensor were plotted as in Fig. 6c and 6d.

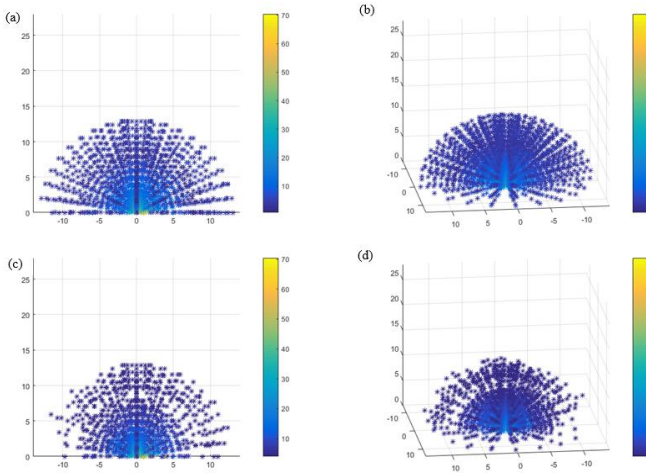

Fig. 6. The 3D plot of commands versus sensing data. The sensing data versus hemispherical coordinates command in X-Y view (a) and X-Y-Z view (b). The sensing data after passing thresholding filter in X-Y view (c), and X-Y-Z view (d).

D. System Overview

The ophthalmic anesthesia training system consists of a rubber manikin, eye phantom, needle, magnetizer and computer as shown in Fig. 1. The eye phantom was embedded with 3D-array hall-effect sensor in the orbital wall. Hall-effect sensors sample magnetic flux from the magnetized needle. A microcontroller unit (MCU) captures data via 12-bit ADC. The sensing data is sent to a computer through UART communication. GUI has been developed using Unity program to calculate and display coordinates of the needle tip relative to ophthalmic anatomy. The 4 fields consist of top view, front view, side view, and 3rd person view.

The eye phantom consists of 3 parts: (1) Orbital structure, (2) Globe and Extraocular muscle, (3) Skin nailing mask. The orbital structure was embedded with a Hall-effect sensor array. The sensor positions were designed in consideration with the retrobulbar pathway as shown in Fig. 7 [1], [2].

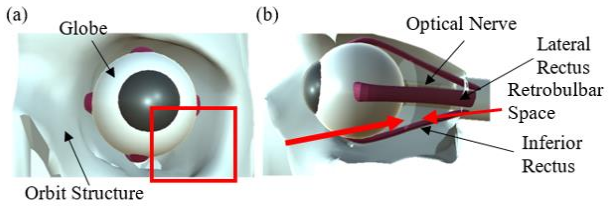

Fig. 7. Ocular anatomy model, operation area of retrobulbar block (Square) (a). Side view of 3D model. Target area of retrobulbar (Arrow) (b).

As a result of the first experiment, the maximum detection range was found to be almost the same as vertical radius of an eye ball (10.5-13.0 mm) [15], [16]. Therefore, the sensor positions have to be considered with the detection range and the shape of sensing workspace. In our related study [17], the simulations of the maximum detection range were simulated in the eye phantom. In current study, the sensing workspaces were simulated on the sensor positions to re-calculate the number of sensors in the orbital structure as shown in Fig. 8. The sensing workspace was simulated using 3ds Max.

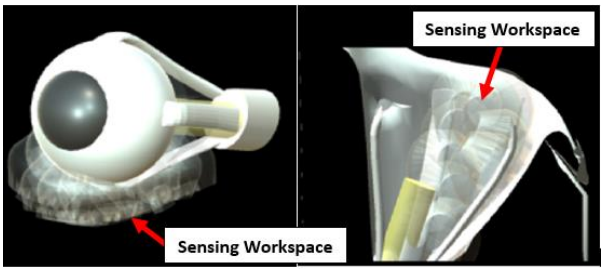

Fig. 8. The 24 workspace simulations of Hall-effect sensor in orbital structure.

The orbital structure was embedded with 24 sensors. The sensor array was designed as 6 columns after considering the sensing workspaces and the wiring holes. The electronic wires passed through the holes behind the sensor sockets as in Fig. 9. The orbital structure, extraocular muscles, optical nerve were produced by 3D printing technique. The FLASHFORGE 3D printer (model CREATOR PRO) was selected with polylactic acid (PLA) material. The skin nailing mask was designed to fix the silicone based artificial skin to the manikin. Artificial skins were used to provide the resistance force to a trainee similar to human skin.

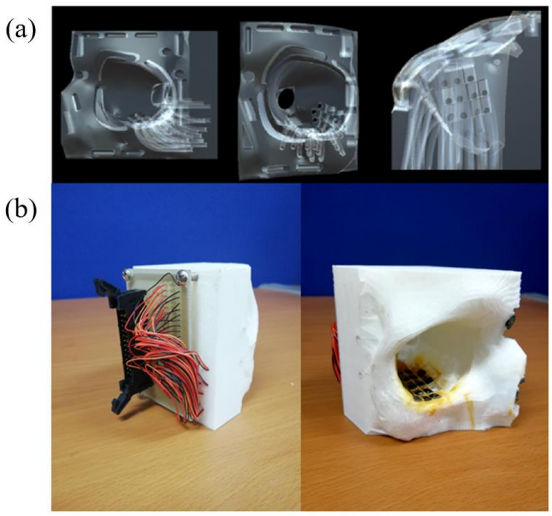

Fig. 9. The developed 3D model of orbital structure with wiring hole (a). The fully assembled orbital structure with embedded sensors (b).

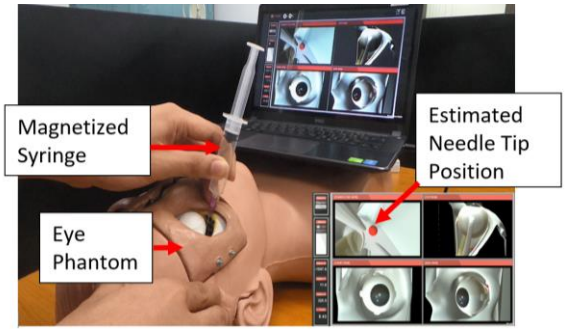

Fig. 10. The developed prototype of magnetic based sensing system for detect magnitized needle by array of Hall-effect sensor.

E. Needle Tip Position Estimation

The sensing data is applied with the thresholding filter as a third experiment. The characterization between the needle tip and the Hall-effect sensor was modeled from the polynomial regression.

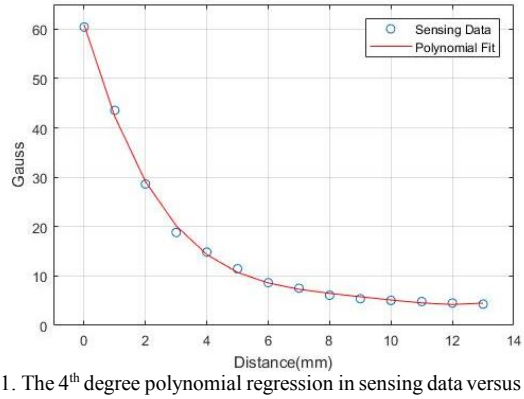

Fig. 11. The 4th degree polynomial regression in sensing data versus distance from sensor for the c experiment.

Fig. 11 shows the 4th degree polynomial plot of the sensing data versus the distances. The coefficients of a polynomial equation are described in Equation (4)

$$h^n = 0.0050{x_n}^4 - 0.2075{x_n}^3 + \\ +3.1308{x_n}^2 - 21.12n + 60.63 \quad (4)$$

where x_n is sensing data of activated sensor n.

The forward kinematic was involved to calculate needle tip position (P_N^n) related to the sensor position (P_S^n). The sensing data from activated sensor n as discussed in Equation (5).

$$P_N^n = {}^N T_S^n \, {}^S T_O^n P_O \quad (5)$$

$${}^N T_S^n = h^n \quad (6)$$

Since the sensor positions had been calculated, the transformation matrixes of the sensors (${}^S T_O^n$) were defined related to the origin frame (P_O). The transformation matrixes between needle tip and sensors (${}^N T_S^n$) is acquired from the characteristic function as in Equation (6). The needle tip can be detected by more than one sensor in the orbital structure, which causes uncertainty of the needle tip position as shown in Fig. 12. The extended Kalman filter (EKF) [18], [19] is

used to estimate the belief position of the needle tip due to the uncertain problem. The EKF algorithm is a general algorithm, which provides the fusion of more than one measurement observed over time to produce the estimates of unknown variables. EKF estimates the needle tip position at time k (X_k) based on the previous position (X_{k-1}), set of measured positions (Z_k) at time k, and set of active sensors (S_{k-1}) at previous time k-1 as in Equation (7, 8, 9).

$$X_k = (X_{k-1}, S_{k-1}) \tag{7}$$

$$Z_k = \{z^1, \dots, z^n\}_k = \{P_N^1, \dots, P_N^n\}_k \tag{8}$$

$$S_{k-1} = \{s^1, \dots, s^n\}_{k-1} = \{{}^S T_O^1, \dots, {}^S T_O^n\}_{k-1} \tag{9}$$

where X represents belief of needle position at time t, X_{t-1} is the previous position of needle tip, S_{k-1} is the coordinates matrixes of n activated sensors and Z_k is the measured position of n activated sensors.

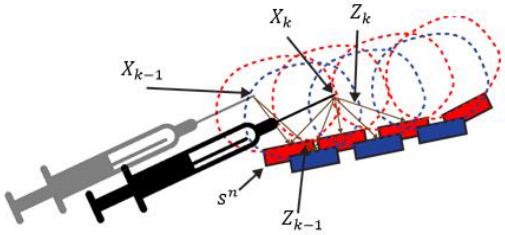

Fig. 12 The uncertainty of the needle tip position due to Hall-effect sensor array.

After considering the overlap of sensing workspaces, the maximum number of activated sensors (n) is limited to 9 (S_k^n, Z_k^n (n= [1,9])), which are sorted by sensing data in descending order. Noise is estimated by Gaussian white noise. A general model can be described by Equation (10, 11).

$$X_k = f\left(X_{k-1}, \{{}^S T_O^1, \dots, {}^S T_O^9\}_{k-1}, \epsilon_k\right) = f(X_{k-1}, (S_k) + \epsilon_{k-1}) \tag{10}$$

$$Z_k = h(S_k, \theta_k) \tag{11}$$

where (f) is the state transition model between previous needle tip position and activated sensor positions, (ϵ_k, θ_k) are the Gaussian white noise of sensor.

Therefore, the needle position at time t (X_k) is calculated from previous position (X_{k-1}) by following the EKF steps.

Algorithm 1: The Needle Tip Localization

Input: Needle tip Positions: $X_{1:k-1} = \{X_1, X_2, \dots, X_{k-1}\}$, Activated Sensor Positions: $S_{1:k} = \{S_1, \dots, S_k\}$, Measured Position: $Z_{1:k}$, Covariance of Needle Position: $P_{1:k-1}$
Output: Needle tip Position: $X_{k|k}$, Covariance error: $P_{k|k}$

Prediction Step:
1: Predicted state estimate: $\hat{X}_{k|k-1} = \hat{X}_{k-1|k-1} + F_k S_k + \epsilon_k$
2: Predicted estimate covariance: $P_{k|k-1} = F_t P_{k-1|k-1} F_k^T + \delta_k$
Update Step:
3: Measurement residual: $\tilde{y}_k = Z_k - H_k \hat{S}_{k|k-1} + \theta_k$
4: Optimal Kalman gain: $K_k = \mathrm{P}_{k|k-1} H_k \left(\theta_k + H_k \mathrm{P}_{k|k-1} H_k^T\right)^{-1}$
5: Update state: $\hat{X}_{k|k} = \hat{X}_{k-1|k-1} + K_k \tilde{y}_k$
6: Update covariance: $P_{k|k} = (I - K_k H_k) P_{k|k-1}$

where K_k is the Kalman gain at time k. F_k is the state estimation model of the needle tip position related to activated sensor positions. H_k is the observation model of needle tip position from sensor data.

F. Accuracy of the Developed System

The experiment was designed to validate the accuracy of the developed system. 8 target coordinates were generated in a 3D model, after considering the anatomical landmarks and the retrobulbar space as in Fig. 13. The coordinates consisted of 3 targets around the inferior rectus muscle and medial rectus muscle, 3 targets in the retrobulbar space, and 2 targets on the orbital structure. The reference point was set at the bottom of the orbital structure. The orbital structure was modified with the marks at the target coordinates using a 3D printer. The target coordinates were sent to the robot manipulator to move the needle tip related to reference point. The needle was initialized at the reference point for 5 seconds to generate the first belief of the EKF algorithm. Then, the needle was moved following the sequence of target coordinates and stopped at each target for 2 seconds. The position of the needle tip was captured as shown in Fig. 14. The experiment was repeated 10 times with the same sequence. The maximum and minimum error in each axis and the root-mean-square error were listed in Table 2.

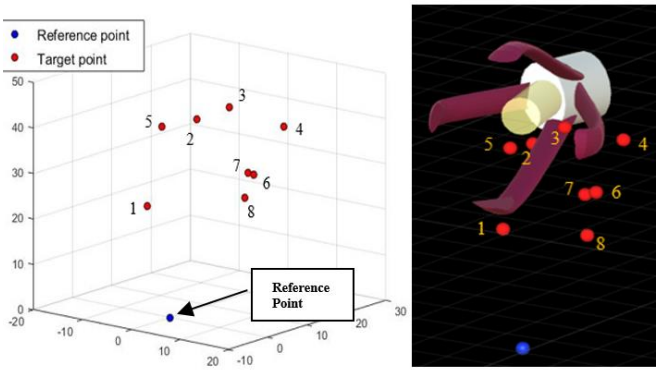

Fig. 13. The 8 target coordinates in orbital structure and reference point.

TABLE II
RANGE OF POSITION COORDINATES FOR 8 TARGET POINTS

Target position	Deviation in System Coordinates (X, Y, Z) (Min: Max in mm unit)	Mean and SD in RMSD (mm)
1	(-1.965: 1.567), (-1.731: 0.777), (-3.097: 4.414)	2.3186, 1.0136
2	(-0.997: 1.342), (-2.095: 0.799), (-3.437: 2.387)	1.8775, 0.8686
3	(-1.158: 1.573), (-1.801: 1.220), (-1.722: 3.736)	2.0457, 1.0275
4	(-0.891: 1.765), (-1.144: 1.939), (-1.114: 1.969)	1.6583, 0.4916
5	(-0.907: 1.405), (-1.057: 1.096), (-0.866: 3.031)	1.4839, 0.8924
6	(-0.849: 0.767), (-1.216: 1.380), (-2.007: 2.051)	1.7528, 0.7700
7	(-0.553: 0.853), (-0.908: 1.522), (-0.616: 4.263)	1.8571, 1.0511
8	(-0.693: 1.058), (-0.831: 1.677), (-1.259: 2.136)	1.4125, 0.5821
	Mean	1.8008
	SD	0.8370

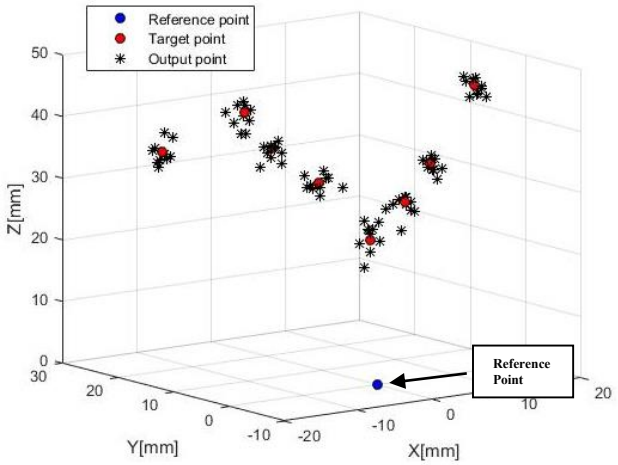

Fig. 14. The calculated coordinates from the EFK algorithm in orbital structure (star points).

III. Conclusions and Discussions

In this study, we found that the magnetization period of an anesthesia needle is longer than the operation time of the ophthalmic anesthesia procedure. The system can perform without any re-magnetized needle during the training period. Additionally, the magnetized needle has high reliability. The changes and re-magnetized process in the needle do not have any major effects on the sensing data ($P<0.05$). The experiments show that the workspace between the magnetized needle and the Hall-effect sensor is a fan-beam shape with maximum detection range of 13 mm. The EKF provides accurate positions with a root-mean-square error around 1.80 mm $\pm$ 0.8370. In addition, the error in x and y axis is smaller (max 1.9 mm) than error in z axis (max 3.7 mm). The system accuracy is less than the commercial product with a magnetic field based tracking system (NDI. Aurora V2 System), which has 1.10 mm in RMS [20]. However, the system has many advantages. The system is simple, deployable, robust and does not require any major changes in the conventional method for eye anesthesia.

As a next step, the system could be developed to estimate the needle orientation using the trajectory of needle tip. Finally, the developed system can be adapted to different platforms of the medical training system that requires a non-modified needle.

Acknowledgment

This project has been supported by Research Development and Engineering, RDE funds NSTDA Thailand. We would like to thank our colleague, Department of Ophthalmology, Faculty of Medicine, Chulalongkorn University and King Chulalongkorn Memorial Hospital (KCMH) for knowledge about medical consultation, and sharing ideas about problems in anesthesia training procedures. The authors thank Miss Choladawan Moonjaita for being project manager and Mr. Shen Treratanakulchai for discussions on electronic components and systems. This research could not be successful without support from the Center for Biomedical and Robotics Technology (BART LAB) of Mahidol University.

References

[1] V. Jaichandran, "Ophthalmic regional anaesthesia: A review and update," *Indian J Anaesth.,* 2013, pp. 7-13.

[2] H. D. Palte, "Ophthalmic regional blocks: management, challenges and solutions," *Local Reg Anesth.,* 2015, pp. 57–70.

[3] T. Eke, and J. R. Thompson, "Serious complications of local anaesthesia for cataract surgery: a 1-year national survey in the United Kingdom," *Br J Ophthalmol.,* 2007, pp. 470–475.

[4] B. J. Adekoya, A. O. Onakoya, B. G. Balogun, and O. Oworu, "Current practice of ophthalmic anesthesia in Nigeria," *Middle East Afr J Ophthalmol.,* 2013, pp. 341–344.

[5] G. Haller, P. S. Myles, P. Taffe, T. V. Perneger, and C. L. Wu, "Rate of undesirable events at beginning of academic year: retrospective cohort study," *Br Med J*., 2009, pp. 3974.

[6] H. A. Schwid, G. A. Rooke, J. Carline, R. H. Steadman, W. B. Murray, M. Olympio, et al., "Evaluation of anesthesia residents using mannequin-based simulation: A multiinstitutional study," *Anesthesiology,* 2002, pp. 1434–1444.

[7] R. Pokroy, E. Du, A. Alzaga, S. Khodadadeh, D. Steen, B. Bachynski, and P. Edwards, "Impact of simulator training on resident cataract surgery," *Graefes Arch. Clin. Exp. Ophthalmol.,* 2013, no. 3, pp. 777–781.

[8] J. R. Merril, N. F. Notaroberto, D. Laby, A. M. Rabinowitz, and T. E. Piemme, "The ophthalmic retrobulbar injection simulator (oris): An application of virtual reality to medical education," in *Proc. Annu. Symp. Computer Application in Medical Care*, 1992, pp. 702-706.

[9] B. Mukherjee, B. George, and M. Sivaprakasam, "An intelligent ophthalmic anesthesia training system based on capacitive sensing," in *Proc. IEEE Int. Instrumentation and Measurement Technology Conf.*, 2013, pp. 889–893.

[10] B. Mukherjee, B. George, and M. Sivaprakasam, "An ophthalmic anesthesia training system using integrated capacitive and Hall effect sensors," *IEEE Trans. Instrum. Meas.*, 2014, no. 5, pp. 1153–1162.

[11] V. Schlageter, P.-A. Besse, R. S. Popovic, and P. Kucera, "Tracking system with five degrees of freedom using a 2D-array of Hall sensors and a permanent magnet," *Sens. Actuators A, Phy.,* 2001, no. 1-3, pp. 37-42.

[12] S. Shijian, Y. Wanan, D. Houde, X. Xuke, L. Mingqiang, S. Bo, and H. Chao, "Investigation of the Relationship Between Tracking Accuracy and Tracking Distance of a Novel Magnetic Tracking System," *IEEE sensor J.,* 2017, no. 15, pp. 4928-4936.

[13] S. Treratanakulchai, K. Borvorntanajanya, C. Moonjaita, and J. Suthakorn, "Needle Tip Position Tracking for Eye Anesthesia Practical Simulator Based on Hall-Effect Array Sensor," *Proceeding of the 20th Annual Conference of the International Society for Computer Aided Surgery (CARS)*, 2016

[14] Allegro MicroSystem Inc. Datasheet of Hall Effect Sensor A1324 "Low Noise, Linear Hall Effect Sensor ICs with Analog Output"

[15] I. Bekerman, P. Gottlieb, and M. Vaiman, "Variations in Eyeball Diameters of the Healthy Adults," *Journal of Ophthalmology,* vol. 2014, Article ID 503645, 5 pages, 2014.

[16] R. C. Augusteyn, D. Nankivil, A. Mohamed, B. Maceo, F. Pierre, and J. -M. Parel, "Human ocular biometry," *Experimental Eye Research J.,* 2012, pp. 70–75.

[17] K. Borvorntanajanya, S. Treratanakulchai, C. Moonjaita, and J. Suthakorn, "The Development of Active Magnetic Field Based Tracking System for Eye Anesthesia Training System," *XXVI Congress of the International Society of Biomechanics, the 9th Asian-Pacific Conference on Biomechanics* (Abstract)*.,* 2017.

[18] R. E. Kalman, "A new approach to linear filtering and prediction problems," Journal of Fluids Engineering, 1960;82, no. 1, pp. 35 – 45.

[19] S. Huang and G. Dissanayake, "Convergence and consistency analysis for extended Kalman filter base slam", *IEEE Trans. Robot.,* 2007, no. 5, pp. 1036-1049.

[20] NDI Medical, Datasheet Electromagnetic Tracking system, "Aurora V2" [Online] Available: http://www.ndigital.com/medical/products/-aurora, 9 Feb 2018.